CHINESE OPTICS LETTERS

Vol. 19, No. 6 | June 2021

Integrated thin film lithium niobate Fabry–Perot modulator [Invited]

Mengyue Xu (徐梦玥), Mingbo He (何名博), Yuntao Zhu (朱运涛), Lin Liu (刘 林), Lifeng Chen (陈立峰)*, Siyuan Yu (余思远)**, and Xinlun Cai (蔡鑫伦)***

State Key Laboratory of Optoelectronic Materials and Technologies and School of Electronics and Information Technology, Sun Yat-sen University, Guangzhou 510000, China

*Corresponding author: chenlf37@mail.sysu.edu.cn

**Corresponding author: yusy@mail.sysu.edu.cn

***Corresponding author: caixlun5@mail.sysu.edu.cn

Received December 25, 2020 | Accepted February 2, 2021 | Posted Online March 24, 2021

Integrated traveling-wave lithium niobate modulators need relatively large device lengths to achieve low drive voltage. To increase modulation efficiency within a compact footprint, we report an integrated Fabry–Perot-type electro-optic thin film lithium niobate on insulator modulator comprising a phase modulation region sandwiched between two distributed Bragg reflectors. The device exhibits low optical loss and a high tuning efficiency of 15.7 pm/V. We also confirm the modulator's high-speed modulation performance by non-return-to-zero modulation with a data rate up to 56 Gbit/s.

Keywords: integrated optic devices; lithium niobate; optical modulators; microstructure fabrication.

DOI: 10.3788/COL202119.060003

1. Introduction

Lithium niobate ($LiNbO_3$, LN) has been the dominant material platform for optical modulators widely used in optical fiber communications due to its excellent physical properties, such as its high electro-optic (EO) Pockels coefficient, low optical absorption, high intrinsic modulation bandwidth, and long-term material reliability[1,2]. However, conventional LN modulators based on low-index-contrast optical waveguides show weak EO interactions, limiting further improvement of modulation efficiency and reduction of device size. Recently, thin film LN-on-insulator (LNOI) has emerged as a promising platform for high-performance integrated modulators, as it offers strong optical confinement and thus high integration density. Several studies have demonstrated the integrated Mach–Zehnder modulators (MZMs) with low drive voltage, low optical insertion loss, and high EO bandwidths on both the LNOI platform[3,4] and silicon-based LN hybrid platform[5–7]. The modulation efficiency of integrated LN modulators with dry-etched LN waveguides has increased to $\sim 2\ \mathrm{V}\cdot\mathrm{cm}$[3,8], which is significantly higher than that of conventional modulators with ion-diffused or proton-exchanged waveguides ($> 10\ \mathrm{V}\cdot\mathrm{cm}$). Even so, an integrated LN modulator in the traveling-wave Mach–Zehnder configuration still has modulation lengths of 1–2 cm to achieve low-voltage energy-efficient modulation. Such footprint sizes are still too large for future optical interconnect applications.

Lumped-element resonant modulators offer smaller device sizes and lower power consumption than traveling-wave MZMs. Various types of resonant LN modulators have been explored, such as micro-ring resonators with circular[9–11] or race-track cavities[12,13] as well as distributed Bragg reflectors (DBRs)[14,15]. Among these, the DBR structure is particularly attractive due to the absence of bending waveguides in resonators, therefore avoiding mode hybridization on an X-cut LN film brought about by the anisotropy of LN material[16]. Another resonant modulator that has not been demonstrated on the LNOI platform is the Fabry–Perot (FP) modulator. The electrical signals modulate the refractive index in the FP cavity, resulting in resonant wavelength shift, thus realizing intensity modulation of transmitted light. FP modulators can offer higher sensitivity because of the sharp roll-offs in its optical transmissivity spectral response.

In this work, we demonstrate an integrated LNOI FP resonator modulator. The on-chip FP cavity is formed by a pair of DBRs as end mirrors and an etched LN waveguide with lumped electrodes between the DBRs. We optimize the design of the DBRs and FP cavity to achieve a low insertion loss (< 1.65 dB) across the whole C band and a high EO tuning efficiency of 15.7 pm/V. Finally, we confirm its performance with non-return-to-zero (NRZ) data modulation up to 56 Gbit/s.

2. Design and Fabrication

Figure 1(a) shows the schematic of the integrated modulator based on the FP resonator. The two DBRs act as mirrors to

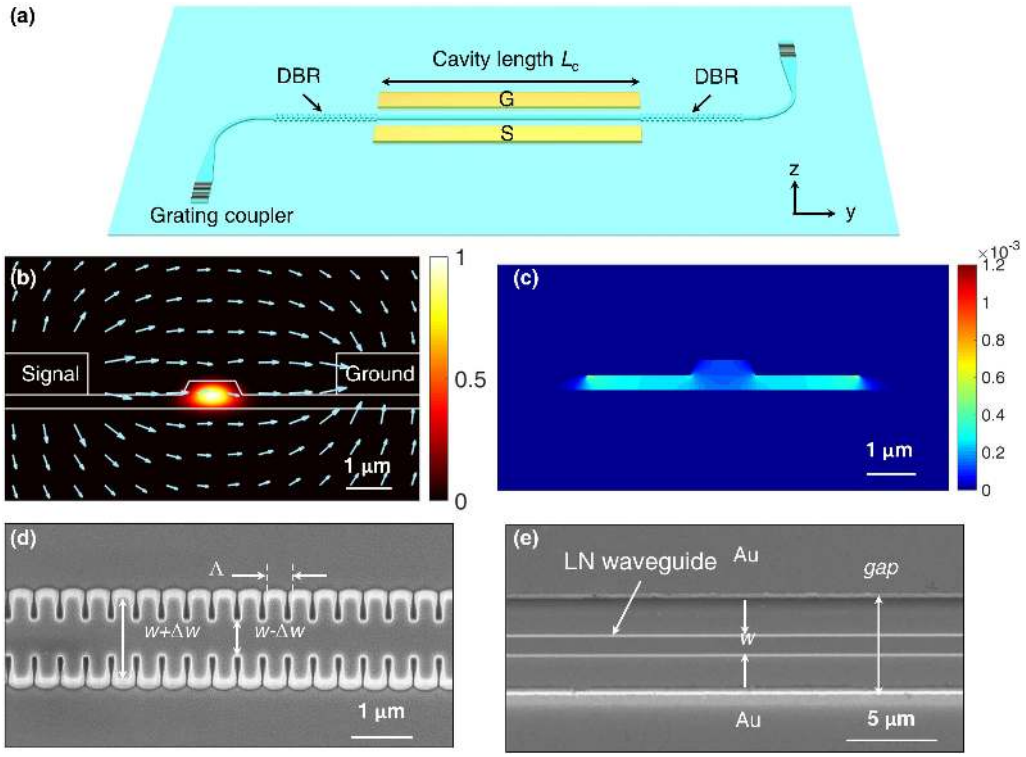

Fig. 1. (a) Schematic of the resonant modulator based on LNOI. (b) Simulated optical TE0 mode profile and electric field distribution. (c) Refractive index change distribution in LN. The applied voltage is 10 V. (d) Scanning electron microscope (SEM) image of the DBR. (e) SEM image of the modulation region.

reflect the light within a particular wavelength range. An EO phase modulator with length L_c is embedded between the DBRs.

Our devices are fabricated on an X-cut LNOI wafer from NANOLN, where a 600 nm thick LN film is bonded on 2.5 μm silicon dioxide. We first define the LN DBR and waveguide patterns using electron-beam lithography (EBL). Next, the ridge waveguides with 300 nm slab thickness are formed by an inductively coupled plasma dry-etching process. Then, we deposit an amorphous-Si (a-Si) layer and define and fabricate a grating coupler in the a-Si layer to ensure efficient fiber-chip coupling and transverse-electric (TE) optical mode operation[17]. Finally, we fabricate the lumped electrodes through a lift-off process. The measured propagation loss of these LN waveguides is about 0.3 dB/cm[8].

We choose the waveguide width in the FP cavity of 1 μm to ensure single-mode operation. In the modulation region, the LN waveguide lays in the gap between the ground and signal (GS) electrodes. As shown in Fig. 1(b), the in-plane electric fields (E_z) between the electrodes are aligned with the z axis of the X-cut LN thin film, so that it can interact with the TE optical mode through the strongest EO coefficient (r_{33}) of LN. When a voltage is applied, the EO effect in the LN material [Fig. 1(c)] causes a change in the effective index (Δn_{eff}) of the optical mode. Figure 2 indicates that the smaller gap of electrodes can bring larger Δn_{eff} and higher absorption loss. We choose the gap of the electrodes as 5.4 μm [Fig. 1(e)] to achieve a negligible metal absorption loss (0.02 dB/cm) and a good overlap between the electric field and optical mode. Figure 1(d) displays the fabricated DBR with a uniform period Λ of 406 nm, an average width w of 1.0 μm, and sidewall corrugation width Δw of 0.5 μm. The Bragg gratings show relatively sharp rectangular shapes, which ensure an essential step effective index modulation.

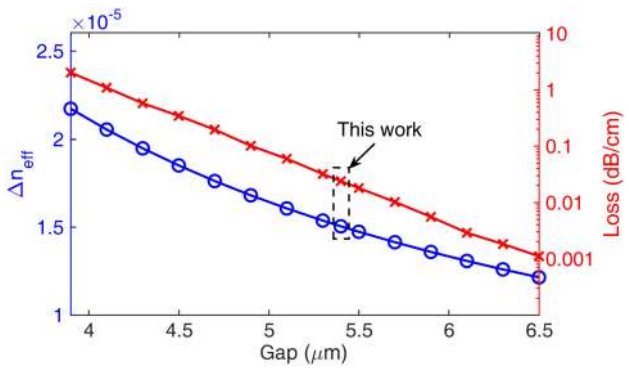

Fig. 2. Variation of the LN waveguide effective refractive index (1 V voltage applied) and absorption loss as a function of the electrode gap.

To optimize the FP modulator for optical interconnects, the design aims for the following.

(1) Broad operating wavelength range, which makes tuning control more flexible.
(2) Maximum modulation efficiency, which minimizes the voltage required to achieve a certain static modulation extinction ratio (ER) at a fixed wavelength.

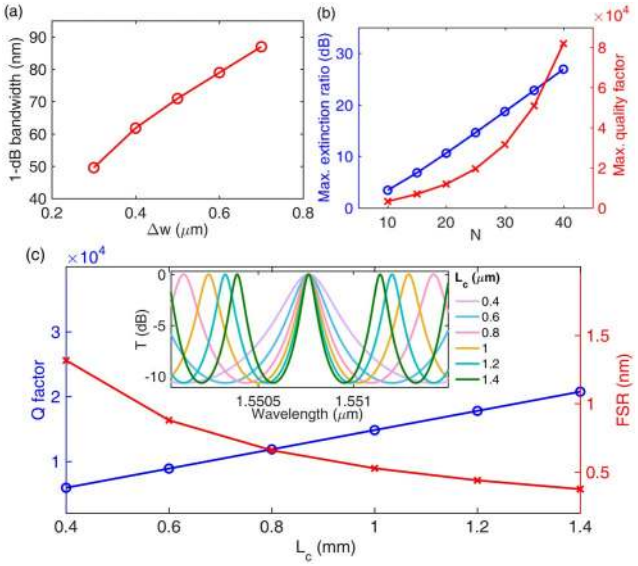

Fig. 3. (a) 1 dB bandwidth of stopband versus corrugation depth Δw. (b) Maximum extinction ratio (ER) and quality (Q) factor versus number of grating periods N. (c) Transmission spectra of the FP modulator with different FP cavity length L_c.

(3) An appropriate trade-off between large static ER and photon-lifetime-limited modulation bandwidth. While a high quality (Q) factor would enable higher ER and lower drive voltage, a lower Q factor would be required to enable higher modulation bandwidth. Most reported resonant modulators have exhibited a Q factor range from 3000 to 14,000 for decent overall performance[9,18–21].

We start the design by choosing a corrugation depth Δw, which determines the operating wavelength range (i.e., the width of the photonic bandgap or stopband). Figure 3(a) shows the 1 dB stopband width as a function of Δw with the number of grating periods $N = 30$ and $\Lambda = 412$ nm. We choose $\Delta w = 0.5\,\mu$m (corresponding to a grating coupling coefficient $\kappa = 113.9\,\mathrm{m}^{-1}$) for a bandwidth of 70 nm. The number of grating periods (N) is also an important parameter, as a high N increases the ER and Q factor [Fig. 3(b)]. According to point (3) mentioned above, we choose N of 20–25 for a smaller Q and an ER larger than 10 dB. Finally, we determine the cavity length L_c, which affects the Q factor and the free-spectral range (FSR). As shown in Fig. 3(c), the Q factor increases with L_c, while the FSR decreases with L_c for $N = 20$. Therefore, the required voltage to switch between the "ON" and "OFF" states decreases with the length of the FP cavity, so does the photon-limited bandwidth. We set L_c at 0.8 mm for a good balance among the modulation efficiency, modulation bandwidth, and footprint.

3. Measurement Results

We measure the normalized transmission spectrum of the FP resonator using a tunable laser (Agilent TLS 81600). The output power of the tunable laser and the wavelength step size are set to 0 dBm and 3 pm, respectively. The measured transmission spectra in Fig. 3 are normalized to the fiber coupling loss. Figure 4(a) indicates that the on-chip insertion loss is less than 1.65 dB across the whole C band. Over the wavelength span of 16 nm, the measured ER is greater than 9 dB. The maximum loaded Q factor of ~12,000 is attained at the Bragg wavelength of ~1548.9 nm, corresponding to a cavity linewidth of 15.6 GHz. The presented device has $N = 30$ for each DBR, which is a little bit more than that of the simulation. Meanwhile, the duty cycle of the fabricated DBR has deviated from the designed 50% [Fig. 1(d)]; hence, the measured stopband bandwidth and reflection are smaller than predicted. Nevertheless, the ER and Q factors meet the performance for the required modulator performance.

To characterize the static EO property of the device, we sweep the DC voltage from 0 V to 25 V while monitoring the shift of resonant wavelengths [Fig. 4(b)]. The resonant wavelength shifts by ~386 pm around 1551.7 nm, exhibiting a linear dependence, as the 25 V voltage is applied with an EO tuning efficiency ($\delta\lambda/\delta V$) of 15.7 pm/V. The presented tuning efficiency is much higher than those of the ring modulator adopted Si/LN (3.3 pm/V[9]) and SiN/LN (2.9 pm/V[13]) hybrid waveguides. For photonic-crystal nanobeam resonators on LNOI[22], the

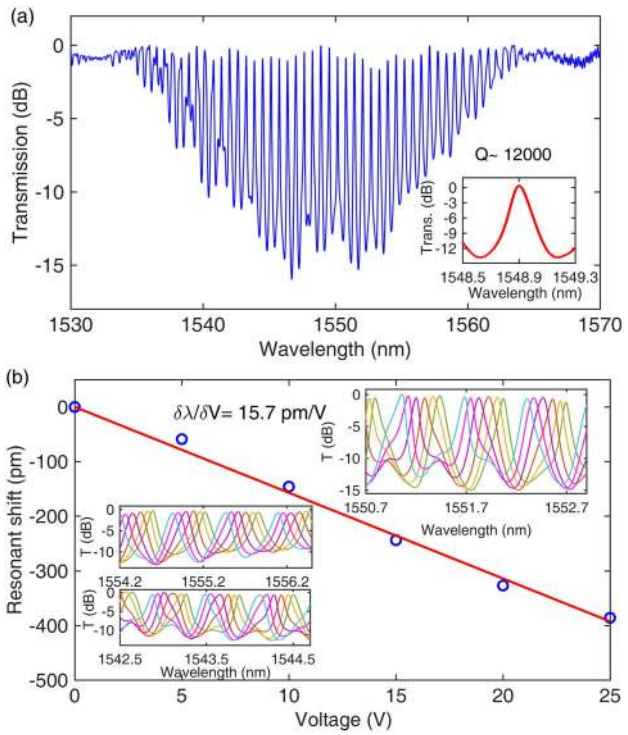

Fig. 4. (a) Measured transmission spectrum of the FP cavity. Inset: the resonance peak at the Bragg wavelength. (b) Measurement and linear fitting of the resonant wavelength shift as a function of the applied DC voltage. Inset: the spectral shift as the voltage sweeps from 0 V to 25 V at different wavelengths.

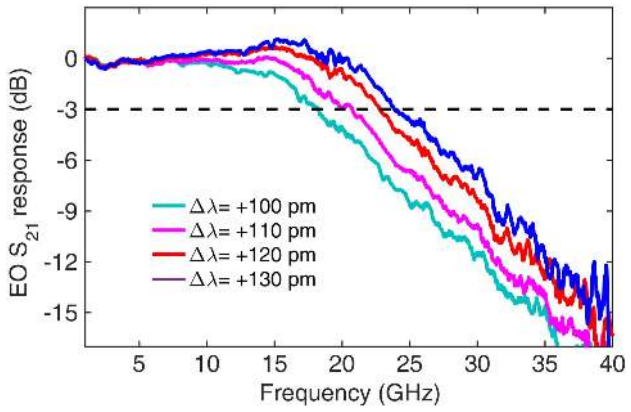

Fig. 5. Measured EO S_{21} responses at different operation wavelengths. $\Delta\lambda$ represents the wavelength offset from the resonance wavelength.

achieved tuning efficiency (16 pm/V) is slightly higher than the one shown here.

To investigate the small-signal response for various optical detuning ($\Delta\lambda$), we measure the EO S_{21} parameters with a vector network analyzer (Agilent N5227A). In Fig. 5, when the wavelength is detuned from 100 pm to 130 pm, the EO bandwidth increases from 18 GHz to 24 GHz. We found that a peak appears before the roll-off, as the optical detuning increases to 120 pm. This peaking effect has been shown to increase the bandwidth beyond the cavity linewidth, but that comes at the expense of reducing the optical modulation amplitude[23–25]. Therefore, we should choose a proper operation wavelength for high-speed modulation.

We verify the high-speed modulation performance with NRZ modulation with the setup shown in Fig. 6(a). A tunable wavelength laser with an optical power of 10 dBm is launched into the modulator. We generate the pseudo-random bit sequences (PRBS) with lengths of $2^{15}-1$ using an arbitrary waveform generator (AWG, Micram). The PBRS signal is amplified by a linear

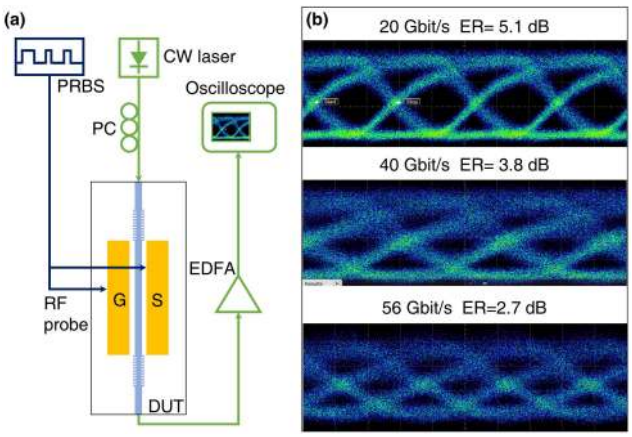

Fig. 6. (a) Experimental setup for measuring the eye diagram. PC, polarization controller; DUT, device under test; EDFA, erbium-doped fiber amplifier; PRBS, pseudo-random binary sequences. (b) Open eye diagrams with data rates of 20, 40, and 56 Gbit/s.

electrical amplifier (SHF 807). Then, the electrical signal with a peak-to-peak voltage of ~3.4 V is applied to the lumped electrodes through a microwave probe. The modulated light is amplified by an erbium-doped fiber amplifier (EDFA) to compensate for the optical insertion loss. The modulated optical signals are recorded by a sampling oscilloscope (DCA, Agilent 86100D) with a 65 GHz optical module. To compensate for the DC bias drift in LN material[26,27], instead of electric DC bias, we tune the input light wavelength at around 1549 nm to achieve the best open eye diagram. The optical eye diagrams at 20 Gbit/s, 40 Gbit/s, and 56 Gbit/s obtain 5.1 dB, 3.8 dB, and 2.7 dB dynamic ER, respectively [Fig. 6(b)]. The dynamic ER decreases as the modulation speed increases because of the limitation of photon-lifetime bandwidth.

4. Conclusion

In summary, we have experimentally demonstrated an LNOI FP resonator modulator. We form the on-chip cavity by integrating two DBRs and an 800 μm modulation region. The fabricated device exhibits a high modulation efficiency of 15.7 pm/V and open eye diagrams up to 56 Gbit/s. Our results suggest a new avenue for utilizing the excellent material properties of LN for very small footprints and a highly efficient optical modulator with good potential in future optical interconnects applications.

Acknowledgement

This work was partially supported by the National Key R&D Program of China (Nos. 2019YFA0705000 and 2019YFB1803900), the National Natural Science Foundation of China (Nos. 11690031 and 11761131001), the Key R&D Program of Guangdong Province (No. 2018B030329001), the Local Innovative and Research Teams Project of Guangdong Pearl River Talents Program (No. 2017BT01X121), the Innovation Fund of WNLO (No. 2018WNLOKF010), and the Project of Key Laboratory of Radar Imaging and Microwave Photonics, Ministry of Education (No. RIMP2019003).

References

1. R. S. Weis and T. K. Gaylord, "Lithium niobate: summary of physical properties and crystal structure," Appl. Phys. A **37**, 191 (1985).
2. A. Honardoost, K. Abdelsalam, and S. Fathpour, "Rejuvenating a versatile photonic material: thin-film lithium niobate," Laser Photon. Rev. **14**, 2000088 (2020).
3. C. Wang, M. Zhang, X. Chen, M. Bertrand, A. Shams-Ansari, S. Chandrasekhar, P. Winzer, and M. Lončar, "Integrated lithium niobate electro-optic modulators operating at CMOS-compatible voltages," Nature **562**, 101 (2018).
4. V. E. Stenger, J. Toney, A. PoNick, D. Brown, B. Griffin, R. Nelson, and S. Sriram, "Low loss and low Vpi thin film lithium niobate on quartz electro-optic modulators," in *2017 European Conference on Optical Communication (ECOC)* (2017), p. 1.
5. M. He, M. Xu, Y. Ren, J. Jian, Z. Ruan, Y. Xu, S. Gao, S. Sun, X. Wen, L. Zhou, L. Liu, C. Guo, H. Chen, S. Yu, L. Liu, and X. Cai, "High-performance hybrid

silicon and lithium niobate Mach–Zehnder modulators for 100 Gbit s^{-1} and beyond," Nat. Photon. **13**, 359 (2019).
6. X. Wang, P. O. Weigel, J. Zhao, M. Ruesing, and S. Mookherjea, "Achieving beyond-100-GHz large-signal modulation bandwidth in hybrid silicon photonics Mach Zehnder modulators using thin film lithium niobate," APL Photon. **4**, 096101 (2019).
7. S. Sun, M. He, M. Xu, X. Zhang, Z. Ruan, L. Zhou, L. Liu, L. Liu, S. Yu, and X. Cai, "High-speed modulator with integrated termination resistor based on hybrid silicon and lithium niobate platform," J. Lightwave Technol. **39**, 1108 (2020).
8. M. Xu, M. He, H. Zhang, J. Jian, Y. Pan, X. Liu, L. Chen, X. Meng, H. Chen, Z. Li, X. Xiao, S. Yu, S. Yu, and X. Cai, "High-performance coherent optical modulators based on thin-film lithium niobate platform," Nat. Commun. **11**, 3911 (2020).
9. L. Chen, Q. Xu, M. G. Wood, and R. M. Reano, "Hybrid silicon and lithium niobate electro-optical ring modulator," Optica **1**, 112 (2014).
10. A. Guarino, G. Poberaj, D. Rezzonico, R. Degl'Innocenti, and P. Günter, "Electro-optically tunable microring resonators in lithium niobate," Nat. Photon. **1**, 407 (2007).
11. A. Rao, A. Patil, J. Chiles, M. Malinowski, S. Novak, K. Richardson, P. Rabiei, and S. Fathpour, "Heterogeneous microring and Mach–Zehnder modulators based on lithium niobate and chalcogenide glasses on silicon," Opt. Express **23**, 22746 (2015).
12. C. Wang, M. Zhang, B. Stern, M. Lipson, and M. Loncar, "Nanophotonic lithium niobate electro-optic modulators," Opt. Express **26**, 1547 (2018).
13. A. N. R. Ahmed, S. Shi, A. J. Mercante, and D. W. Prather, "High-performance racetrack resonator in silicon nitride–thin film lithium niobate hybrid platform," Opt. Express **27**, 30741 (2019).
14. M. R. Escalé, D. Pohl, A. Sergeyev, and R. Grange, "Extreme electro-optic tuning of Bragg mirrors integrated in lithium niobate nanowaveguides," Opt. Lett. **43**, 1515 (2018).
15. M. R. Escalé, D. Pohl, W. Heni, B. Baeuerle, A. Josten, A. Sergeyev, J. Leuthold, and R. Grange, "Integrated electro-optic Bragg modulators in lithium niobate nanowaveguides," in *Advanced Photonics 2018* (2018), paper IW4I.4.
16. J. Wang, P. Chen, D. Dai, and L. Liu, "Polarization coupling of X-cut thin film lithium niobate based waveguides," IEEE Photon. J. **12**, 2200310 (2020).
17. J. Jian, P. Xu, H. Chen, M. He, Z. Wu, L. Zhou, L. Liu, C. Yang, and S. Yu, "High-efficiency hybrid amorphous silicon grating couplers for sub-micron-sized lithium niobate waveguides," Opt. Express **26**, 29651 (2018).
18. X. Xiao, X. Y. Li, H. Xu, Y. T. Hu, K. Xiong, Z. Y. Li, T. Chu, J. Z. Yu, and Y. D. Yu, "44-Gb/s silicon microring modulators based on zigzag PN junctions," IEEE Photon. Technol. Lett. **24**, 1712 (2012).
19. G. Li, A. V. Krishnamoorthy, I. Shubin, J. Yao, Y. Luo, H. Thacker, X. Zheng, K. Raj, and J. E. Cunningham, "Ring resonator modulators in silicon for interchip photonic links," IEEE J. Sel. Top. Quantum Electron. **19**, 3401819 (2013).
20. T. Baba, S. Akiyama, M. Imai, N. Hirayama, H. Takahashi, Y. Noguchi, T. Horikawa, and T. Usuki, "50-Gb/s ring-resonator-based silicon modulator," Opt. Express **21**, 11869 (2013).
21. Y. Tong, Z. Hu, X. Wu, S. Liu, L. Chang, A. Netherton, C. Chan, J. E. Bowers, and H. K. Tsang, "An experimental demonstration of 160-Gbit/s PAM-4 using a silicon micro-ring modulator," IEEE Photon. Technol. Lett. **32**, 125 (2019).
22. M. Li, J. Ling, Y. He, U. A. Javid, S. Xue, and Q. Lin, "Lithium niobate photonic-crystal electro-optic modulator," Nat. Commun. **11**, 4123 (2020).
23. J. Muller, F. Merget, S. S. Azadeh, J. Hauck, S. R. Garcia, B. Shen, and J. Witzens, "Optical peaking enhancement in high-speed ring modulators," Sci. Rep. **4**, 6310 (2014).
24. H. Yu, D. Q. Ying, M. Pantouvaki, J. Van Campenhout, P. Absil, Y. L. Hao, J. Y. Yang, and X. Q. Jiang, "Trade-off between optical modulation amplitude and modulation bandwidth of silicon micro-ring modulators," Opt. Express **22**, 15178 (2014).
25. M. Bahadori, Y. Yang, A. E. Hassanien, L. L. Goddard, and S. Gong, "Theory of coupled harmonics and its application to resonant and non-resonant electro-optic modulators," J. Lightwave Technol. **38**, 5756 (2020).
26. J. P. Salvestrini, L. Guilbert, M. Fontana, M. Abarkan, and S. Gille, "Analysis and control of the DC drift in $LiNbO_3$-based Mach–Zehnder modulators," J. Lightwave Technol. **29**, 1522 (2011).
27. S. Sun, M. He, M. Xu, S. Gao, Z. Chen, X. Zhang, Z. Ruan, X. Wu, L. Zhou, L. Liu, C. Lu, C. Guo, L. Liu, S. Yu, and X. Cai, "Bias-drift-free Mach–Zehnder modulators based on a heterogeneous silicon and lithium niobate platform," Photon. Res. **8**, 1958 (2020).